

# DyRA: Portable Dynamic Resolution Adjustment Network for Existing Detectors

Daeun Seo<sup>1</sup>, Hoeseok Yang<sup>2</sup>, Hyungshin Kim<sup>1</sup>

<sup>1</sup> Chungnam National University, Republic of Korea

<sup>2</sup> Santa Clara University, USA

**Abstract.** Achieving constant accuracy in object detection is challenging due to the inherent variability of object sizes. One effective approach to this problem involves optimizing input resolution, referred to as a multi-resolution strategy. Previous approaches to resolution optimization have often been based on pre-defined resolutions with manual selection. However, there is a lack of study on run-time resolution optimization for existing architectures. This paper introduces *DyRA*, a dynamic resolution adjustment network providing an image-specific scale factor for existing detectors. This network is co-trained with detectors utilizing specially designed loss functions, namely *ParetoScaleLoss* and *BalanceLoss*. *ParetoScaleLoss* determines an adaptive scale factor for robustness, while *BalanceLoss* optimizes overall scale factors according to the localization performance of the detector. The loss function is devised to minimize the accuracy drop across contrasting objectives of different-sized objects for scaling. Our proposed network can improve accuracy across various models, including RetinaNet, Faster-RCNN, FCOS, DINO, and H-Deformable-DETR.

**Keywords:** Image Resolution · Scale Robustness · Object Detection

## 1 Introduction

Deep learning has demonstrated remarkable performance in computer vision applications such as object detection [43, 57] and segmentation [1, 38]. However, achieving consistent accuracy in real-world applications remains a challenge due to the variability of instance sizes [8, 29, 56]. The variation in size is often significant in object detection, which can cause the robustness of accuracy vulnerable [46]. Several solutions have been proposed to address this problem, either by optimizing the architecture of neural networks [29, 30, 34] or by augmenting the input data [35, 46, 47]. In data augmentation, resolution adjustment can effectively address the problem without changing the network architecture.

Fig. 1 illustrates why varying image resolution can improve detection accuracy. Due to the scale-variant performance of detection networks, objects with extreme sizes, either large or small, are not well identified. To alleviate this shortcoming, resizing the image containing huge or tiny objects to a lower or higher resolution, i.e., matching the resolution to the original capacity of the detector,

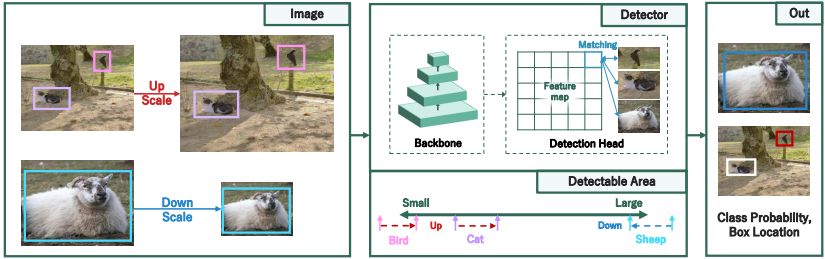


**Fig. 1:** Motivation for judicious image scaling. Scaling the resolution to align with the network’s capacity can enhance the detection accuracy of extreme scales.

can help the network recognize objects more efficiently. If the resolution of the image can be properly adjusted, the accuracy of the detection will be effectively enhanced, which is the main focus of this work. Moreover, a careful resolution selection can lead the network to extract richer information since the resolution is a crucial hyper-parameter for the performance of networks [48, 49].

There are several approaches to optimizing the resolution, which can be classified into three: The first is to scale the input images with *predefined* resolutions and apply them as data-augmentation to the networks [35, 46], which is also applicable to transformer-based networks [36, 37, 50, 63]. The dynamic resolution network [68] allows adaptive resolution by selecting one of these sizes. However, an obvious drawback of this approach is that it requires manual work to determine candidate resolutions, relying on expert knowledge with lots of trial and error. To eliminate such need for human expertise, the second approach, *automated augmentation search* [8], has been proposed to enable an optimized resolution for each image or box. The last is the *run-time adaptive scaling* [21], which optimizes the resolution on the fly without domain-specific knowledge.

In this paper, we propose a portable run-time adaptive scaling network called *DyRA*, which produces an image-specific scale factor. Fig. 2a illustrates how the proposed image scaler can be plugged into an existing detector. Note that the input to the scaler module is the image, while its output is a single scale factor for the resolution. *DyRA* is designed as a separate companion neural network with convolution and transformer blocks and is jointly trained with a conventional object detector. By jointly training these two networks, the scale factor can be optimized to maximize the performance of the detector while learning the input-specific scale factor.

When training *DyRA*, two newly designed loss functions are applied, which are depicted in Fig. 2b. The image typically includes several different-sized objects, which makes it hard to decide the scale factor to provide accuracy gain for all instances. Hence, *ParetoScaleLoss* aims to minimize the accuracy drop caused by the size variation by employing Pareto optimality [9] and Maximum Likelihood Estimation (MLE) [39] from *ScaleLoss*, which is for box-specific scale factor. The optimization of the box-level scale factor is executed by enlarging or reducing it based on the given box size. *BalanceLoss* modifies the overall scale

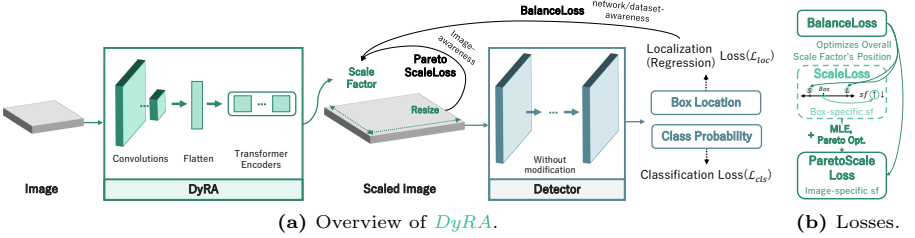


**Fig. 2:** (a) The overall architecture consists of two networks: *DyRA* and the detector. First, *DyRA* aims to estimate the scale factor from the given image; then, the detector classifies and localizes objects from the resized image as a general inference process. The proposed network is optimized by two additional loss functions, which are *ParetoScaleLoss* and *BalacneLoss*. (b) *ParetoScaleLoss* optimizes an image-specific scale factor based on *ScaleLoss*, which decides a box-specific scale factor. These loss functions adjust the factor based on the relative location within the boundary sizes for up-/down-scaling. *BalanceLoss* modifies the boundaries based on the detector’s localization performance.

factor’s position based on the localization performance to have a network-aware scale factor. Through these loss functions, the scale factor can be optimized for scale robustness while considering the performance of the detector.

Different from prior approaches, *DyRA* provides high portability to existing detectors without domain-specific knowledge about the input data once after the training. For instance, the automatic scaling decision in Hao et al. [21] is not transferable to other detectors because the entire neural network is adapted by the resized image. To the best of our knowledge, *DyRA* is the first attempt to dynamically optimize the hyper-parameter in a fully separable network from existing networks in an end-to-end manner. Furthermore, our network yields a continuous scale factor that offers extensive scale coverage, resulting in higher detection performance. This is crucial because selecting from a few discrete sizes can lead to a distribution mismatch due to the continuous range of the resolution.

We verified the effectiveness of the proposed approach with various object detectors on MS-COCO [32], PascalVOC [15], and DOTA [60]. In COCO, detectors achieved an AP (average precision) improvement of 1.4% on RetinaNet [31], 1.0% on Faster R-CNN [44], 1.5% on FCOS [52], 1.5% on DINO [6], and 1.2% on H-deforamble-DETR [26] compared to the multi-resolution strategy. In PascalVOC and DOTA, the AP of Faster-RCNN enhanced by 1.8% and 2.3%, respectively.

## 2 Related Work

**Object Detection Networks.** The object detector is a model that identifies and localizes objects from images, which consists of three components, namely a backbone, a neck, and a head. The backbone is responsible for extracting features from the image, so pre-trained image classifiers such as [23, 48, 61] are widely used. The neck [17, 30, 34, 67] extracts multi-scale features utilized in the subsequent

detection procedure. The head receives these features as input and finalizes the detection process, which has two approaches: One-stage [3, 31, 35, 43, 55] and two-stage [18, 22, 44, 57]. One-stage networks can achieve low inference latency with a unified head architecture, while two-stage networks have relatively high latency due to additional refinement networks. To get rid of anchors, anchor-free detectors [14, 52, 62, 64] were introduced, which don't require non-maximum suppression (NMS) [41]. As an emerging self-attention [53], transformer-based detectors [5, 6, 26, 70] were suggested and showed high performance. Since our method is based on image scaling, it is agnostic to the mentioned detection topologies.

**Image-level Multi-resolution Strategies.** As stated earlier, several previous works take multiple resolutions into account. 1) Predefined multi-resolution: The simplest way is to apply a set of multiple resolutions as a data augmentation [35, 46, 47]. This provides high applicability, including transformer-based detectors. For transformers, multi-resolution patchification [2] has been proposed with the same objectivity. The dynamic resolution selection technique [68] is also based on predefined resolutions and selects one from the resolutions. 2) Automated data augmentation: Cubuk et al. [10, 11] proposed image augmentation techniques that automatically combine color- and resolution-based augmentation. Based on this, Chen et al. [8] proposed box-/image-level augmentation to deal with scale variance. 3) Run-time scaling: Hao et al. [21] presented a run-time resolution prediction network in a single-scale region proposal network (RPN) for a face detection application.

**Dynamic Neural Networks.** Dynamic neural networks [20] refer to network architectures or parameters that can be adaptively reconfigured on the fly. In this area, the goal of networks can be divided into two aspects: improving representational power and reducing latency. A kernel-wise dynamic sampling [12, 16, 69] in convolutions enables an adaptive receptive field, which improves the representation capabilities. A dynamic activation function [7] can enhance the ability with adaptive piece-wise linear activation. In a coarser view, feature-level dynamic attention [24, 27] provides channel-wise attention by weighting salient features. For multi-scale architecture, branch-wise soft attention network [56] provides additional information in an image-specific approach. Channel skipping [25, 28] is also proposed for low inference latency while executing only crucial channels. Early exiting [4, 13, 42, 58] is a method that exits the layer after achieving a sufficient result. In object detection, the dynamic early exit [33, 66] was adopted by cascading multiple backbone networks.

### 3 Dynamic Resolution Adjustment: *DyRA*

#### 3.1 Overall Architecture

The overall architecture of the proposed technique is depicted in Fig. 2a, where *DyRA* is positioned between the input image and the original object detector. In the absence of *DyRA*, the detector  $\mathbf{D}$  predicts box locations and classes directly from the input image  $\mathcal{I}$  as  $\mathcal{Y} = \mathbf{D}(\mathcal{I})$ . The suggested methodology aims to

enhance detection accuracy while taking a non-intrusive approach to prioritize portability. In other words, we keep *DyRA* agnostic to the original detector by modifying the input image  $\mathcal{I}$  to  $\mathcal{I}'$  for a better detection output,  $\mathcal{Y}'$ , where  $\mathcal{Y}' = \mathbf{D}(\mathcal{I}')$ .

We introduce an image-wise scale factor to optimize the resolution, which is effectively predictable by the network, in contrast to a box-wise scale factor. This is because the box-wise scale factor requires additional layers or multiple inference processes to detect salient regions to scale. The image  $\mathcal{I}$  is modified with a scale factor  $\phi$  as,

$$\mathcal{I}' = \text{Scale}(\mathcal{I}, \phi), \quad (1)$$

where *Scale* is an image scaling operation that makes the width and height of  $\mathcal{I}'$  become  $\phi \cdot \mathcal{I}_W$  and  $\phi \cdot \mathcal{I}_H$ , respectively. The objective of *DyRA* is to determine the scale factor,  $\phi$ , that maximizes the performance of  $\mathcal{Y}'$ , surpassing that of  $\mathcal{Y}$ .

As illustrated in Fig. 2a, *DyRA* consists of two modules: The first component consists of convolutional layers that extract features from the image. The following component is for predicting the scale factor with transformer encoder layers and a fully connected layer. We utilized lightweight CNNs and only a 1-D vector for the transformer module, resulting in a negligible computation overhead for the detector. These components produce raw scale factors from the image, denoted as  $\phi_{raw}$ . From the raw scale factor, *DyRA* utilizes sigmoid activation function  $\sigma$  to normalize to a range of  $[0, 1]$ ; then, to establish the lower and upper bounds of the scale factor, we employ a tunable parameter  $\tau$  that confines the scale factor within the range  $[\tau^2/10, \tau]$ . This procedure can be represented as follows:

$$\phi = \max(\sigma(\phi_{raw}), \tau \cdot 10^{-1}) \cdot \tau. \quad (2)$$

In this study, we selected the value of  $\tau$  as 2, which led to the minimum of  $\tau^2 \cdot 10^{-1} = 0.4$  and the maximum of 2.

### 3.2 Proposed Loss functions of *DyRA*

**Scale Factor of Single Object (*ScaleLoss*)** As mentioned in Fig. 1, scaling up for small and down for large objects is required to enhance accuracy. Hence, the scale factor should be optimized in two directions: increasing the scale factor for small objects and decreasing it for large objects. Based on the inversely proportional relationship between the scale factor and the object size, we define the loss function  $\mathcal{L}_{scale}$ , which determines the scale factor of the individual object. The Binary Cross Entropy (BCE) loss, similar to our optimization scheme, conducts bi-directional optimizations based on the label  $y$ <sup>3</sup>. This loss function can be utilized to modify the scale factor, such as  $\mathcal{L}_{BCE}(y, \phi)$ , by assigning  $y = 0$  for large objects and  $y = 1$  for small objects.

<sup>3</sup>  $\mathcal{L}_{BCE}(y, \hat{y}) = -\frac{1}{N} \sum^N (y \log(\hat{y}) + (1 - y) \log(1 - \hat{y}))$ , where  $y$  and  $\hat{y}$  are the label and estimated probability from a classifier. The probability  $\hat{y}$  is optimized in two directions: increasing the probability  $\hat{y}$  for the positive label ( $y = 1$ ) and decreasing it for the negative label ( $y = 0$ ).

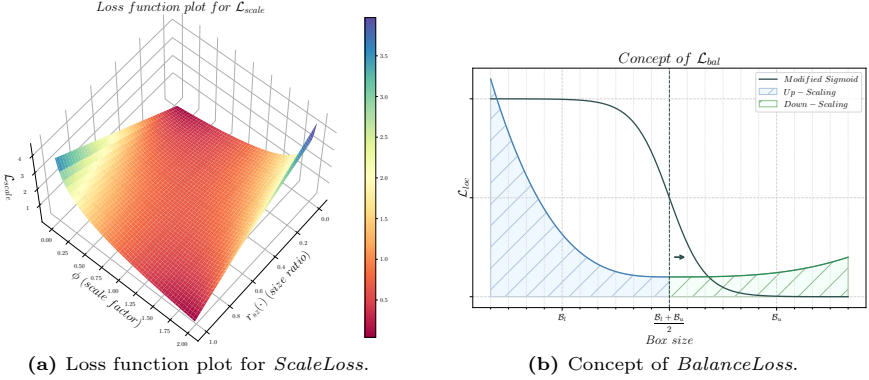


**Fig. 3:** (a) The  $x$ -axis denotes the size ratio, and the  $y$ -axis is the predicted scale factor from *DyRA*. The network is optimized by two additional loss functions, which are *ParetoScaleLoss* and *BalacneLoss*. (b) By the average of  $\mathcal{B}$ , boxes are divided into two groups: blue (to be upscaled) and green (to be downscaled). If the loss value of the blue region is larger than the green, the  $\mu(\mathcal{B})$  will be moved to the right to reduce the loss value of the blue region.

In this context, a size ratio  $r_{sz}(\cdot)$  is devised, which is a normalized box size ranging from 0 to 1 for utilizing as the label  $y$ . Previous approaches [5, 52] to box size normalization typically involve size adjustments based on architectural components, but they rely on a specific architecture or can result in inaccurate scale factors due to the diversity of the component, i.e., the image resolution. Instead, we apply the box size directly to preserve the information by inputting the size into the sigmoid function. The sigmoid function necessitates an additional operation on the input data to obtain the box size as input<sup>4</sup>.

Due to the high variation and unpredictability of box sizes, determining the appropriate size range is challenging. Therefore, we introduce a size boundary  $\mathcal{B} = \langle \mathcal{B}_l, \mathcal{B}_u \rangle$ , representing the mini-/maxi-mum of threshold in  $x$ -axis in the sigmoid, which is defined by a learnable parameter as will be elaborated later. The modified sigmoid function for domain  $[\mathcal{B}_l, \mathcal{B}_u]$  is illustrated as grayline in Fig. 3b. This function returns horizontally a mirrored output for a result close to 0 for large and 1 for small objects.

Based on the range, the size ratio is specified as,

$$r_{sz}(b) = \sigma_{\mathcal{B}}(b_{\mathcal{W}} \cdot b_{\mathcal{H}}), \quad (3)$$

where  $b_{\mathcal{W}}$  and  $b_{\mathcal{H}}$  are the width and height of the box  $b$ , and  $\sigma_{\mathcal{B}}$  is a modified sigmoid function with respect to  $\mathcal{B}$ . In this modified sigmoid, the size greater (or

<sup>4</sup> The sigmoid returns  $\sigma(x) = 1$  when  $x \geq 6$  and  $\sigma(x) = 0$  when  $x \leq -6$ , but this narrow range of  $x$ -values is not suitable for the box size input, necessitating modification for the input data  $x$ .

smaller) than the upper (or lower) bound is saturated to 0.0 (or 1.0) as,

$$\sigma_{\mathcal{B}}(x) = \begin{cases} 0.0 & x > \mathcal{B}_u \\ \sigma(-x) & \mathcal{B}_l \leq x \leq \mathcal{B}_u \\ 1.0 & x < \mathcal{B}_l \end{cases}. \quad (4)$$

Then, *ScaleLoss* is defined as,

$$\mathcal{L}_{scale}(b, \phi) = -(r_{sz}(b') \log(\frac{\phi}{\tau}) + (1 - r_{sz}(b')) \log(1 - \frac{\phi}{\tau})), \quad (5)$$

where  $b'$  is a resized box by the scale factor  $\phi$ . The difference from the BCE is the scale factor for medium-sized boxes, which don't necessitate an extreme value, such as 2.0 or 0.4. For these objects, we directly use the size ratio as the label to decide the scale factor from all terms in Eq. (5). As displayed in Fig. 3a, a local minimum of  $\mathcal{L}_{scale}$  has formed in the proportional relationship between the size ratio and the scale factor. The loss function  $\mathcal{L}_{scale}$  is minimized when a large size ratio increases the scale factor  $\phi$ ; conversely, a small ratio decreases  $\phi$ .

**Considering Multiple Objects (*ParetoScaleLoss*)** When the image contains multiple objects, an appropriate scale factor for one instance may not be suitable for others due to the high variation in object sizes. The practice of averaging *ScaleLoss* functions over several items may not be feasible due to the potential accuracy degradation on a small number of scales. Alternatively, we adopt a Pareto optimality [9] that can incorporate various scales, as in SA-AutoAug [8]. The scale factor is selected to minimize accuracy degradation over a set of scales  $\mathbb{S}$ , which controls the trade-off in size variation.

With cumulated *ScaleLoss*  $\mathcal{L}_{scale}^i$  for boxes belong to  $i \in \mathbb{S}$ , this objective can be formulated as,

$$\min_{\phi} f_{i \in \mathbb{S}}(\mathcal{L}_{scale}^i). \quad (6)$$

From the MLE [39] perspective, minimizing the objective function Eq. (6) is equivalent to maximizing the likelihood of the function, which is defined as follows:

$$\max_{\phi} \mathcal{P} = \max_{\phi} \prod_{i \in \mathbb{S}} \mathcal{P}_{scale}^i = \max_{\phi} \prod_{i \in \mathbb{S}} e^{-f(\mathcal{L}_{scale}^i)}. \quad (7)$$

where  $\mathcal{P}$  is the likelihood. The difference from Eq. (6) is that each *ScaleLoss* is connected by a multiplication, which allows joint optimization across  $\mathbb{S}$ , as in Zhang et al. [65].

With scalar-valued  $f(\cdot)$ , a log-likelihood is applied to the final *ParetoScaleLoss* as,

$$\mathcal{L}_{PS}(b, \phi) = -\log(\mathcal{P}) = -\log\left(\prod_{i \in \mathbb{S}} e^{-\frac{1}{N_i} \mathcal{L}_{scale}^i}\right), \quad (8)$$

where  $N_i$  is the number of boxes in scale  $i$ . In this process, the scaled box  $b'$  is applied when grouping boxes. The subset of base anchors is adopted as the scales  $\mathbb{S}$ , as representative sizes of objects in the dataset.

**Adjustment of Overall Scale Factor (*BalanceLoss*)** In *ScaleLoss*, the scale factor is decided based on the specified range  $\mathcal{B}$ . The definition of the range  $\mathcal{B}$  is modified by incorporating a learnable parameter  $\gamma$  as follows:

$$\mathcal{B} = \langle \mathcal{B}_l, \mathcal{B}_u \rangle = \langle \gamma \cdot \tilde{\mathcal{B}}_l, \gamma \cdot \tilde{\mathcal{B}}_u \rangle. \quad (9)$$

In what follows, we present the loss function, *BalanceLoss*, which can adaptively adjust the threshold  $\mathcal{B}$  by optimizing  $\gamma$ . The modification of the threshold results in an alteration of the overall scale factor’s position. To align scale factors with the detector’s capability, we modify the threshold based on the representation power of the original network. This procedure enables the optimization of scale factors in a performance-aware manner while learning the scale robustness by *ParetoScaleLoss*.

*BalanceLoss* aims to find a balanced threshold between the performance of boxes. To simplify the problem, we compare the localization performance between box subsets, as shown in Fig. 3b. Boxes are divided into two groups, which necessitate either up-scaling( $\mathcal{G}_u$ ) or down-scaling( $\mathcal{G}_d$ ). Based on an average  $\mu(\mathcal{B})$  of the threshold  $\mathcal{B}$ , a smaller or larger box than  $\mu(\mathcal{B})$  is considered as it requires up- or down-scaling, respectively. We measure the performance based on the averaged localization loss, denoted as  $\mu(\mathcal{L}_{loc}^{\mathcal{G}})$  for a subset  $\mathcal{G}$ . It is possible to obtain the balanced threshold by minimizing the difference between the localization losses of subsets. For instance, if  $\mu(\mathcal{L}_{loc}^{\mathcal{G}_u})$  is higher than  $\mu(\mathcal{L}_{loc}^{\mathcal{G}_d})$ , it is desirable to increase the  $\mu(\mathcal{B})$  to decrease the loss of  $\mathcal{G}_u$ .

This strategy can be formulated as,

$$\mathcal{L}_{bal}(\mathcal{B}) = \|\mu(\mathcal{B}), \frac{\langle \mu(\mathcal{L}_{loc}^{\mathcal{G}_d}), \mu(\mathcal{L}_{loc}^{\mathcal{G}_u}) \rangle \cdot \langle \mathcal{T}_d, \mathcal{T}_u \rangle}{2}\|_1, \quad (10)$$

where  $\langle \mathcal{T}_d, \mathcal{T}_u \rangle$  are target boundaries of each subset for  $\mu(\mathcal{B})$ . The averaged loss values are multiplied element-wise with the boundaries  $\langle \mathcal{T}_d, \mathcal{T}_u \rangle$  and summed together by the dot product ‘ $\cdot$ ’. If one of the subsets exhibits a higher loss value, the summed value will be shifted to the corresponding boundary of the subset. To modify the  $\gamma$ , Eq. (10) is divided by the average  $\mu(\tilde{\mathcal{B}})$  as,

$$\mathcal{L}_{bal}(\mathcal{B}) = \|\gamma, \frac{\langle \mu(\mathcal{L}_{loc}^{\mathcal{G}_d}), \mu(\mathcal{L}_{loc}^{\mathcal{G}_u}) \rangle \cdot \langle \mathcal{T}_d, \mathcal{T}_u \rangle}{2 \cdot \mu(\tilde{\mathcal{B}})}\|_1, \quad (11)$$

because of  $\mu(\mathcal{B}) = \frac{\gamma(\tilde{\mathcal{B}}_l + \tilde{\mathcal{B}}_u)}{2}$ . If the pair  $\langle \mathcal{T}_d, \mathcal{T}_u \rangle$  is sufficiently large and small, the  $\gamma$  can be converged within two values. We select the  $\langle \mathcal{T}_d, \mathcal{T}_u \rangle$  as the second big-/small-est base anchor sizes, while  $\langle \tilde{\mathcal{B}}_l, \tilde{\mathcal{B}}_u \rangle$  are chosen as threshold sizes in the AP metric, which identify small/large objects.

Since the typical loss value is under 1.0, this small loss value can lead to training the threshold to be tiny, not for balanced performance. Therefore, we apply a normalization function to the loss value, a modified Mean-Max function in Free-Anchor [65], which results in sensitive output within the input range of  $0.1 \leq x \leq 0.9$ . The mean-max function is revised to produce the respective



**Algorithm 1:** Training process

---

**Input** : Image  $\mathcal{I} \in \mathcal{R}^{C \times H \times W}$ ; Image batch  $\mathcal{B}$  and  $n$  is the number of batches; Ground truth box sizes  $\mathbb{B}_{\mathcal{I}}$  in the  $\mathcal{I}$

- 1 **for**  $\mathcal{I}_i \in \mathcal{B}$  where  $i \in (1 \text{ to } n)$  **do**
- 2      $\phi_i \leftarrow DyRA(\mathcal{I}_i)$ ; // Predict scale factor  $\phi$
- 3      $\mathcal{I}'_i \leftarrow Scale(\mathcal{I}_i, \phi_i)$ ; // Resize images by the scale factor
- 4     **for**  $b \in \mathbb{B}_{\mathcal{I}'_i}$  **do**
- 5          $\mathcal{L}_{scale}^b \leftarrow ComputeScaleLoss(b, \phi_i)$ ;
- 6     **end**
- 7      $\mathcal{L}_{PS}^{\mathcal{I}'_i} \leftarrow ComputeParetoScaleLoss(\mathbb{B}_{\mathcal{I}'_i}, \mathcal{L}_{scale}^{\mathbb{B}_{\mathcal{I}'_i}})$ ;
- 8 **end**
- 9  $\mathcal{I}' \leftarrow Preprocessing(\mathcal{I}'_1, \dots, \mathcal{I}'_n)$ ; // Preprocess images into one tensor
- 10  $\mathcal{Y}, \mathcal{L}_{cls}, \mathcal{L}_{loc} \leftarrow Detector(\mathcal{I}')$ ;
- 11  $\mathcal{L}_{PS} \leftarrow \frac{1}{n} \sum_{i=1}^n \mathcal{L}_{PS}^{\mathcal{I}'_i}$ ; // Averaging ParetoScaleLoss over batches
- 12  $\mathcal{L}_{bal} \leftarrow ComputeBalanceLoss(\mathcal{L}_{loc}, \mathbb{B}_{\mathcal{B}})$ ;

**Output:** Losses  $(\mathcal{L}_{cls}, \mathcal{L}_{loc}, \mathcal{L}_{PS}, \mathcal{L}_{bal})$ , Prediction  $\mathcal{Y}$

---

output from an input  $\mathbf{x}$  as follows:

$$Norm(\mathbf{x}) = \frac{f(x)}{\sum_{x \in \mathbf{x}} f(x)}, \quad f(x) = \frac{1}{1 - x} \quad (12)$$

The normalization is executed before computing *BalanceLoss* for localization loss functions.

### 3.3 Total Loss Function

The detector is trained with classification loss ( $\mathcal{L}_{cls}$ ) and localization (regression) loss ( $\mathcal{L}_{loc}$ ) as in Fig. 2a. Generally, the total loss function is defined as a weighted sum of all loss functions, such as  $\mathcal{L}_{total} = \mathcal{L}_{cls} + \mathcal{L}_{loc} + \mathcal{L}_{PS} + \mathcal{L}_{bal}$ . It is desirable to associate the convergence of *DyRA* with the detector to facilitate joint training. For this purpose, an additional weight is applied to the newly designed loss functions, which is the localization loss value as,

$$\mathcal{L}_{total} = \mathcal{L}_{cls} + \mathcal{L}_{loc} + \mathcal{L}_{loc}^* \cdot (\mathcal{L}_{PS} + \mathcal{L}_{bal}). \quad (13)$$

The loss value  $\mathcal{L}_{loc}^*$ , which is applied as the weight, doesn't execute a gradient update to preserve the original meaning of loss functions. Through the weight, *DyRA* can avoid harming the convergence of the detector caused by different convergence speeds to the detector.

In the case of two-stage detectors, each stage produces the loss function, i.e.,  $\mathcal{L}_{loc} = (\mathcal{L}_{loc}^1, \dots, \mathcal{L}_{loc}^n)$ , utilized in *BalanceLoss*. In this case, *BalanceLoss* is modified with the corresponding localization loss in each stage as,

$$\mathcal{L}_{bal}^{stage} = -\log(\mathcal{P}_{bal}^{stage}) = -\log\left(\prod_{i \in stage} e^{-\mathcal{L}_{loc}^{i*} \cdot \mathcal{L}_{bal}^i}\right), \quad (14)$$

Dataset	Model <sup>stage</sup>	Backbone	Policy	AP	AP <sub>50</sub>	AP <sub>75</sub>	AP <sub>s</sub>	AP <sub>m</sub>	AP <sub>l</sub>	Iterations
COCO	RetinaNet <sup>1</sup> (anchor-base)	ResNet50	Baseline	36.6	55.7	39.1	20.8	40.2	49.4	-
			MS baseline	38.7	58.0	41.5	23.4	42.3	50.3	270k
			MS baseline <sup>†</sup>	38.6	58.1	41.6	22.5	42.5	49.6	180k
			<i>DyRA</i> <sup>†</sup>	<b>40.1</b>	<b>60.0</b>	<b>42.5</b>	<b>25.5</b>	<b>43.1</b>	<b>52.6</b>	<b>180k</b>
		ResNet101	Baseline	38.8	59.1	42.3	21.8	42.7	50.2	-
			MS baseline	40.4	60.3	43.2	24.0	44.4	52.2	270k
			<i>DyRA</i> <sup>†</sup>	<b>41.6</b>	<b>61.5</b>	<b>44.8</b>	<b>25.1</b>	<b>45.5</b>	<b>53.7</b>	<b>180k</b>
	Faster-RCNN <sup>2</sup> (anchor-base)	ResNet50	Baseline	37.6	57.8	41.0	22.2	39.9	48.4	-
			MS baseline	40.2	61.0	43.8	24.2	43.6	51.9	270k
		<i>DyRA</i> <sup>†</sup>	<b>41.2</b>	<b>62.3</b>	<b>44.8</b>	<b>25.4</b>	<b>44.0</b>	<b>54.5</b>	<b>180k</b>	
		ResNet101	Baseline	39.8	57.8	41.0	23.1	43.2	52.3	-
	MS baseline		42.0	62.5	45.9	25.2	45.6	54.6	270k	
	<i>DyRA</i> <sup>†</sup>	<b>42.9</b>	<b>63.3</b>	<b>46.4</b>	<b>26.0</b>	<b>46.2</b>	<b>56.1</b>	<b>180k</b>		
	FCOS <sup>1</sup> (anchor-free)	ResNet50	MS baseline	41.0	59.9	44.2	25.0	45.3	51.7	180k
<i>DyRA</i> <sup>†</sup>		<b>42.5</b>	<b>61.3</b>	<b>46.3</b>	<b>27.3</b>	<b>45.7</b>	<b>54.8</b>	<b>180k</b>		
ResNet101		MS baseline	43.1	62.0	46.8	27.9	47.0	55.1	180k	
		<i>DyRA</i> <sup>†</sup>	<b>44.1</b>	<b>63.4</b>	<b>47.8</b>	<b>28.5</b>	<b>47.5</b>	<b>57.0</b>	<b>180k</b>	
DINO-4scale <sup>1</sup> (transformer)	ResNet50	MS baseline	49.2	66.7	53.8	32.3	52.5	63.6	90k	
		AMP baseline	49.0	66.3	53.4	31.4	52.3	63.3	90k	
<i>DyRA</i> <sup>†</sup>	<b>50.5</b>	<b>67.9</b>	<b>55.3</b>	<b>34.3</b>	<b>52.7</b>	<b>64.1</b>	<b>90k</b>			
H-Deformable-DETR <sup>2</sup> (transformer)	ResNet50	MS baseline	49.1	67.0	53.7	32.2	52.3	63.8	90k	
		AMP baseline	48.6	66.7	52.8	31.3	52.0	63.4	90k	
<i>DyRA</i> <sup>†</sup>	<b>49.8</b>	<b>67.9</b>	<b>54.7</b>	<b>34.2</b>	<b>52.5</b>	<b>63.1</b>	<b>90k</b>			
PascalVOC	Faster-RCNN-C4 <sup>2</sup> (without FPN)	ResNet50	MS baseline	51.9	80.3	56.6	-	-	-	18k
			<i>DyRA</i> <sup>†</sup>	<b>54.6</b>	<b>81.2</b>	<b>59.9</b>	-	-	-	<b>18k</b>
	Faster-RCNN <sup>2</sup>	ResNet50	MS baseline	54.5	82.1	60.5	-	-	-	18k
			<i>DyRA</i> <sup>†</sup>	<b>56.2</b>	<b>82.5</b>	<b>62.4</b>	-	-	-	<b>18k</b>
DOTAv1.5	Faster-RCNN <sup>2</sup>	ResNet50	MS Baseline <sup>†</sup>	36.2	58.6	38.7	18.8	39.5	43.9	250k
			Baseline-OBb [19]	-	62.0	-	-	-	-	130k
			<i>DyRA</i> <sup>†</sup>	<b>38.5</b>	<b>62.7</b>	<b>40.7</b>	<b>22.9</b>	<b>42.3</b>	<b>44.8</b>	<b>250k</b>

**Table 1:** Accuracy comparison on COCO minival, PascalVOC, and DOTAv1.5. (1: one-stage, 2: two-stage, MS: multi-scale, †: train with *ConstCosine* scheduling).

with the MLE form in Eq. (7). For *ParetoScaleLoss*, the weight can be obtained by the likelihood of localization losses with the same technique as in Eq. (14). Thus, the total loss function for the two-stage detector is defined as,

$$\mathcal{L}_{total}^{stage} = \mathcal{L}_{cls} + \mathcal{L}_{loc} - \mathcal{L}_{PS} \cdot \log(\mathcal{P}_{loc}^{stage*}) + \mathcal{L}_{bal}^{stage}. \quad (15)$$

## 4 Experiments

### 4.1 Implementation Details

For the learning rate, *ConstCosine* scheduling is applied, which combines constant and half-cosine scheduling<sup>5</sup>. The multi-resolution training is used for *DyRA*, which scales the image within a range of 640-800 while maintaining an aspect

<sup>5</sup>  $lr = \min(2 \cos(\min(\frac{4}{3} \frac{iter}{max\_iter} - \frac{\pi}{3})), 0) + 2$ .

ratio of images. All detectors are trained in a 4-GPU environment with 16 image batches, except for DOTA, which uses 1 batch size. Images of DOTA are split into the size of 1024 with a 768 sliding window. Transformers are trained with Automatic Mixed Precision (AMP) [40]. For COCO and PascalVOC, accuracies of baselines were borrowed from frameworks [45, 51, 59] and SA-AutoAug [54].

## 4.2 Accuracy Improvement

Our proposed method shows its applicability to various object detectors and datasets, as reported in Tab. 1. The AP scores of detectors improved by nearly 1.0% simply by training with *DyRA*. For CNN-based detectors, FCOS on ResNet50 achieved the highest AP improvement, 1.5%, while RetinaNet and Faster-RCNN show enhancements of 1.4% and 1.0%, respectively. The improvement is clearly visible for  $AP_s$  and  $AP_l$  as expected from our method’s fundamental intuition in Fig. 1. In FCOS,  $AP_s$  and  $AP_l$  were notably bigger (2.3% and 2.9% respectively). We also applied *DyRA* to transformer-based detectors and obtained accuracy gains of 1.3%, and 0.7% for DINO and H-deformable-DETR, respectively. When comparing models with the AMP baseline, our network can acquire 1.5% and 1.2% accuracy gain, leading to a fair comparison to our network. Although these transformer-based detectors already reached a high AP score of nearly 49%, the proposed method could enhance its accuracy further with about a 2.0% increase in  $AP_s$ . In overall detectors, one-stage detectors demonstrated more gain than the two-stage detectors when adopting our network.

Accuracy was improved by 2.7% and 1.7% over the MS baseline in PascalVOC without and with FPN, respectively. Faster-RCNN-C4 shows the highest improvement among the detectors, indicating that our method is more effective when the original detector shows a relatively low and scale-variant accuracy. This score exceeds the accuracy of the FPN-based MS baseline by 0.1% without architectural modification. In DOTA, Faster-RCNN shows the highest improvement among the datasets, 2.3% in AP and 3.9% in  $AP_{50}$ , due to the fact that the objects in this dataset are highly scale-variant. This result is 0.7% higher than the baseline with oriented bounding box (OBB) [19], known as effective for the aerial dataset.

## 4.3 Analysis of Scale Factors

Fig. 4 illustrates the distribution of scale factors obtained from *DyRA* with respect to the image’s averaged object sizes. As intended in the definition of *ScaleLoss*, the trained image scaler produces low-scale factors for large objects and high-scale factors for small objects. In the right images, the scale factor is lower than 0.5 for images only containing huge objects and higher than 1.9 for images with tiny instances. For scale factors around 1.0, the image contains medium-sized objects (e.g., the 4th image only contains a keyboard), or large and small objects together (e.g., the 1st image contains a dog and a bed together). This shows that *DyRA* can find the scale factor that minimizes the accuracy drop. In the scale distribution, there are a few outliers in the upper right of the

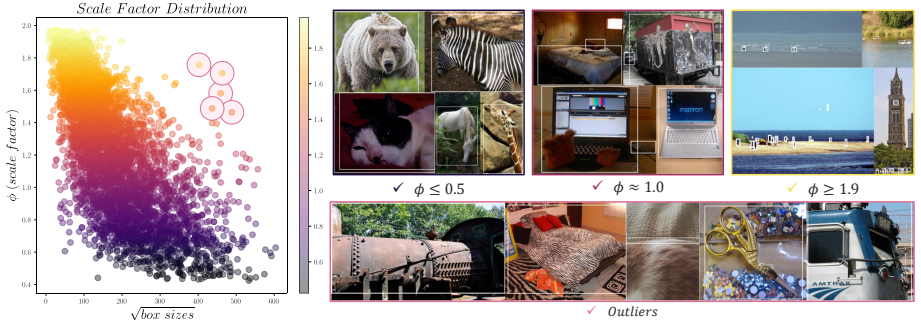


**Fig. 4:** Distribution of scale factors and examples of images. The  $x$ -axis is a square root of averaged box sizes within each image in the COCO.

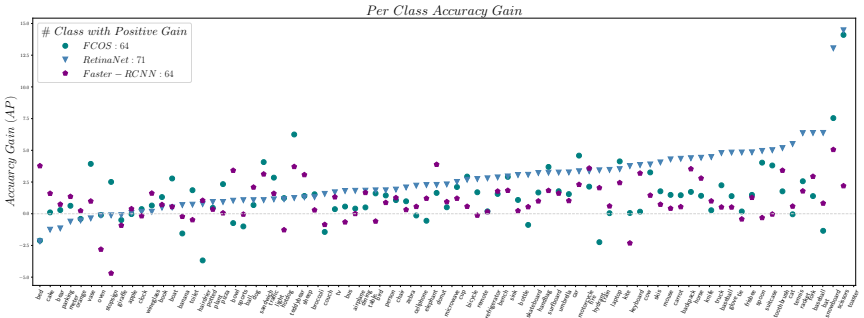


**Fig. 5:** Accuracy gain of each class of COCO trained with various detectors with *DyRA*.

graph. As the number of outliers is marginal, it can be said that our network has the adaptability to handle objects with size variation.

We measured per-class accuracy to better comprehend the impact of the scale factor in Fig. 5. The  $y$ -axis represents the AP gain of *DyRA* compared to the MS baseline, while the  $x$ -axis denotes classes in COCO. For all detectors, most of the classes exhibit accuracy growth. RetinaNet shows the largest number of classes of positive gain, 71, with the highest AP improvement of 14.46%. The number of classes with negative gains is only 9, with the lowest gain of -2.5%, which is  $0.17\times$  lower than the highest gain. Both Faster-RCNN and FCOS achieved the AP gain across 64 classes, with the highest gains of 5.05% and 14.10%, respectively.

Tab. 2 displays the common classes with the highest or lowest AP gain for detectors in Fig. 5. There are only 2 common negative classes, whereas the number of positive classes is 59 for all 3 detectors. The highest gain for positive classes is  $10.3\times$  greater than the lowest negative gain, -1.0%. The images in positive classes consist of various-sized objects, while the corresponding objects are small-sized. For example, the first image contains toasters with large objects, such as the desk. This shows that the obtained scale factor can improve the accuracy of small objects within images that contain many large objects, which indicates

Gain (#CLS.)	Classes (Averaged Gain (%))
Positive (49)	toaster (10.3), scissors (8.5), teddy bear (3.7) ...
Negative (2)	oven (-1.0), giraffe (-0.5), -

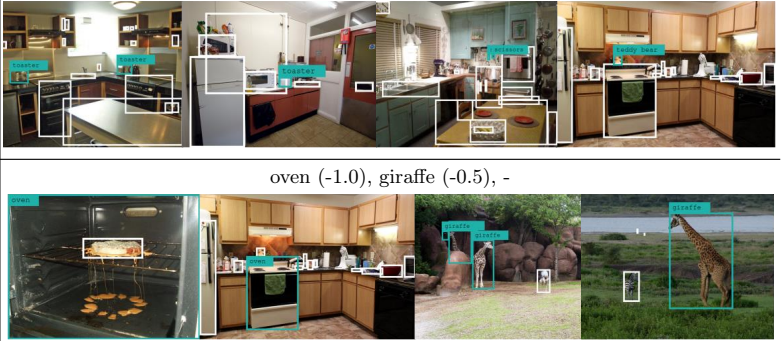


**Table 2:** Top-3 common classes with high-/low-est accuracy gain for detectors in Fig. 5. The blue bounding box indicates the corresponding class’s object.

our scale factor can consider the minority of scales in one scene. In contrast, the objects with negative gain are relatively large within the image containing small objects, such as in the second image. This image is the same as the last image in positive gain, which indicates that the small accuracy degradation occurred from the contract sizes of objects. Since the degradation occurred only in 2 classes, the majority of objects can achieve accuracy gain while minimizing the accuracy drop by employing Pareto optimality.

#### 4.4 Ablation study

**Comparison with SA-AutoAug.** We performed a comparative evaluation of the proposed method with SA-AutoAug [8] in Tab. 3. *DyRA* attained an equivalent AP to SA-AutoAug after training 180k iterations, with 1.5% higher  $AP_s$ . The SA-AutoAug requires 20 GPU days in the Tesla V100 (2.5 days with 8 GPUs) to find scale factors, but our method only requires 2 GPU days in the RTX A6000. By joint training with the detector, our network can get a much lower cost to find scale factor than the search. The cost of *DyRA* is obtained by subtracting 0.5 days (without *DyRA*) from 1 day (with *DyRA*).

Model	Method	AP	$AP_s$	$AP_m$	$AP_l$	Iterations	Strategy	Fine-tune	Cost of SF
RetinaNet (R50, COCO)	SA (img-level)	40.1	24.0	<b>44.1</b>	<b>53.1</b>	540k	Search	Needed	20 GPU-days
	<i>DyRA</i>	40.1	<b>25.5</b>	43.1	52.6	180k	DynamicNN	×	2 GPU-days

**Table 3:** Comparison with SA-AutoAug (SF: scale factor, SA: SA-AutoAug).

**Computation cost.** As shown in Tab. 4, *DyRA* has 3M parameters and takes 13 GFLOPs to get the scale factor, which is about 7% of the complexity of Faster-RCNN. These results are measured with an image resolution of 800.

Model <sup>◊</sup>	Param.	Comput.	Model	Param. (% of ◊)	Comput. (% of ◊)
Faster-RCNN	40M	180 GFLOPs	<b>DyRA</b>	<b>3M (7.5%)</b>	<b>13 GFLOPs (7.2%)</b>

**Table 4:** Computation cost compared with the Faster-RCNN.

**Per-box Localization power.** In order to verify our primary hypothesis, the detector has relatively low performance on objects with extreme sizes, we measured the per-box localization loss in FCOS models. The 3-layer baseline exhibits higher loss at two endpoints, whereas the 5-layer baseline shows only high loss at small objects due to the effectiveness of the 5-layer in detecting large objects. Applying **DyRA** to the baseline model (2nd col) resulted in decreased average and standard deviation across all scales, particularly for small instances.

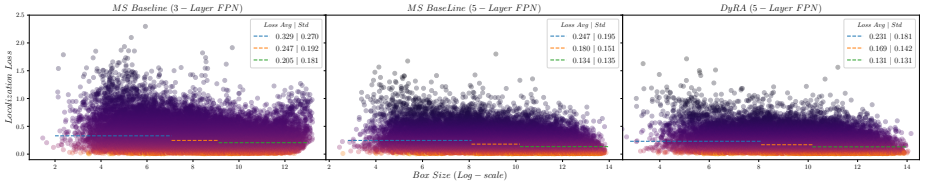


**Fig. 6:** Per box localization loss on FCOS (ResNet50). Boxes are equally divided into 3 groups, indicating **small**, **medium**, and **large** objects.

**Effect of *BalanceLoss*.** Fig. 7a illustrates the training process with or without *BalanceLoss*, which adjusts the overall position of scale factors by modifying  $\gamma$ . Excluding *BalanceLoss* leads to an increased  $\gamma$  without convergence, causing the scale factor trained to raise its value. With *BalanceLoss*, the scale factor can learn scale robustness in a stable environment with converged  $\gamma$ . Fig. 7b shows the finalized  $\gamma$  value, which exhibits an inverse relationship with the  $AP_s$  of baseline models. This implies that our *BalanceLoss* can determine the performance-specific threshold.

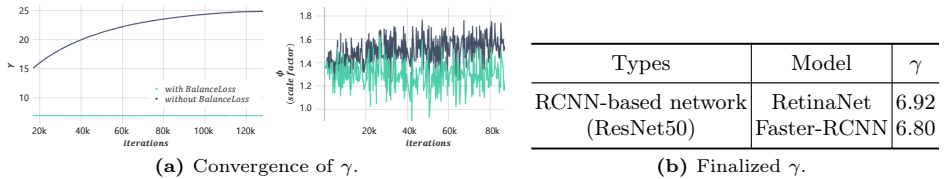


**Fig. 7:** (a) *BalanceLoss* can help to converge  $\gamma$ . (b) Network-specific  $\gamma$ .

Tab. 5 displays 0.2% lower AP of model without *BalanceLoss*. Too high  $\gamma$  results in damaging the detection performance of both small and large objects.

Model	$\gamma$	AP	AP <sub>50</sub>	AP <sub>75</sub>	AP <sub>s</sub>	AP <sub>m</sub>	AP <sub>l</sub>
RetinaNet	24.78 (without <i>BalanceLoss</i> )	39.9	60.0	42.5	24.3	43.1	52.0
(ResNet50)	<b>6.92 (with <i>BalanceLoss</i>)</b>	<b>40.1</b>	<b>60.0</b>	<b>42.5</b>	<b>25.5</b>	<b>43.1</b>	<b>52.6</b>

**Table 5:** Accuracy of model training without *BalanceLoss*s.

**Pareto optimality.** In *ParetoScaleLoss*, the scale  $\mathbb{S}$  is selected as the subset of base anchors. The experiment in several subsets is presented in Fig. 8a. Without

optimality, the model shows relatively low  $AP_s$ , which indicates Pareto optimality is effective for scale robustness. The small sizes of  $\mathbb{S}$  exhibit the highest accuracy due to the low detection performance for small objects shown in Fig. 6. As  $\mathbb{S}$  with various sizes penalizes for the adaptiveness of scale factors as shown in Fig. 8b,  $\mathbb{S}$  with all sizes displays a lower AP than small sizes.

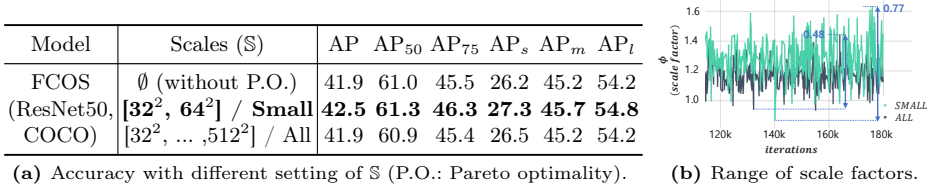


**Fig. 8:** (a) P.O. can help to detect small objects. (b) The small-sized scales  $\mathbb{S}$  exhibit higher adaptiveness of scale factors in training process.

**Effect of Proposed Loss Functions.** We designated *ParetoScaleLoss* and *BalanceLoss* to enhance the robustness of accuracy by alleviating the scale variation. We conducted experiments on a model with only the architecture of *DyRA* without the proposed loss functions to understand their impact on accuracy in Fig. 9b. The accuracy of DINO without proposed losses shows a 2.8% lower AP than the model with proposed losses. The lack of proposed losses results in the limited adaptiveness of scale factors as expressed in Fig. 9a, which leads to low performance of the detector.

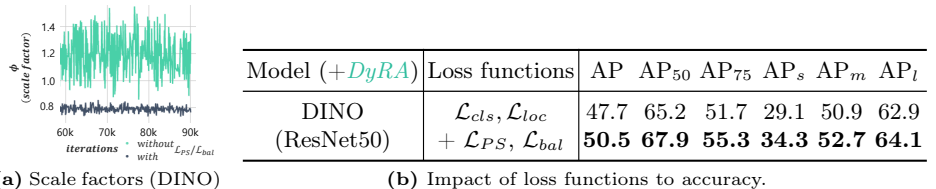


**Fig. 9:** (a) Scale factors over training iterations. (b) The absence of proposed loss functions significantly reduces the accuracy of DINO.

**Weight of Proposed Losses.** We incorporated localization loss  $\mathcal{L}_{loc}^*$  as the weight of proposed loss functions, *ParetoScaleLoss* and *BalanceLoss*, as discussed in a Sec. 3.3. Due to both activated terms in *ScaleLoss*, *ParetoScaleLoss* does not much decrease across all iterations, as exhibited in Fig. 10a. By  $\mathcal{L}_{loc}^*$  (variable weight), *ParetoScaleLoss* is reduced notably compared to utilizing without any weight. Also, convergence slopes between the two settings show a similar characteristic, which implies the variable weight also does not interfere with the convergence of our network. Fig. 10b illustrates the difference between localization losses during training. In initial iterations, the model without weight shows a lower localization loss than the variable weight model, but the variable weight model exhibits a higher number of lower losses across the overall training phase.



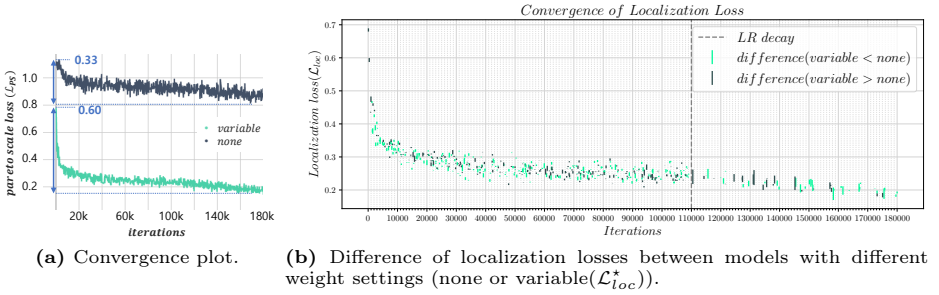


**Fig. 10:** (a) Convergence of *ParetoScaleLoss* in RetinaNet. (b) The bar indicates the difference in localization losses between two different settings in RetinaNet. The gray bar indicates that the model without weight shows a lower localization loss, while the green bar denotes that the model with variable weight produces a lower value.

**ConstCosine Learning Rate Scheduling.** Our network generates a continuous range of scale factors, making conventional discrete learning rate (LR) scheduling unsuitable for *DyRA*, such as a step function. Therefore, *ConstCosine* LR scheduling is utilized to achieve a smooth transition, as illustrated in Fig. 11a. This method can result in higher accuracy than the multi-step method, as shown in Fig. 11b. The enhancement by *CC* scheduling is more noticeable in Faster-RCNN, which is trained with a high LR of 0.02. Otherwise, DINO shows a low effect on *CC* scheduling due to the robustness of the LR transition because of the low LR value.

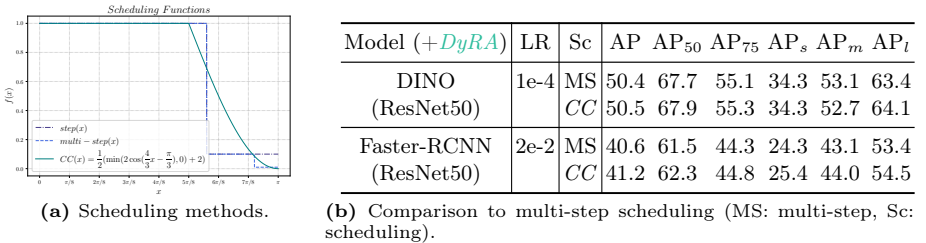


**Fig. 11:** (a) Scheduling function plot. (b) Obtained accuracy from multi-step and *ConstCosine* learning rate scheduling.

**Effect of Multi-scale Training.** We employed multi-scale (MS) resolution for training *DyRA* with detectors. To understand the impact of MS training on *DyRA*, we conduct training with only a single resolution (800), as shown in Tab. 6. The accuracy achieved by both models is comparable, with a slight 0.1% advantage in the single resolution. However, we opted for the MS setting to get faster training speeds.

Model (+ <i>DyRA</i> )	Train augment.	$\tau$	AP	AP <sub>50</sub>	AP <sub>75</sub>	AP <sub>s</sub>	AP <sub>m</sub>	AP <sub>t</sub>
FCOS (ResNet50)	MS (640-800)	2	42.5	61.3	46.3	27.3	45.7	54.8
	Single (800)	2	42.6	61.5	46.5	27.1	45.8	54.4

**Table 6:** Impact of data augmentation.



## 5 Conclusion & Limitation

This paper presents a network called *DyRA* designated to adjust image resolution for scale robustness in object detection. The proposed method is portable to existing networks and provides the image-specific scale factor, which can achieve at least a 1.0% gain for well-known detection datasets. However, since the proposed method uses image-wise rather than box-wise scaling, it tends to cause overhead for large-scale factors. Currently, we only consider object detection in this work, which lacks generality for various tasks. This remains a future work.

## References

1. Badrinarayanan, V., Kendall, A., Cipolla, R.: Segnet: A deep convolutional encoder-decoder architecture for image segmentation. *IEEE transactions on pattern analysis and machine intelligence* **39**(12), 2481–2495 (2017) [1](#)
2. Beyer, L., Izmailov, P., Kolesnikov, A., Caron, M., Kornblith, S., Zhai, X., Minderer, M., Tschannen, M., Alabdulmohsin, I., Pavetic, F.: Flexivit: One model for all patch sizes. In: *Proceedings of the IEEE/CVF Conference on Computer Vision and Pattern Recognition*. pp. 14496–14506 (2023) [4](#)
3. Bochkovskiy, A., Wang, C.Y., Liao, H.Y.M.: Yolov4: Optimal speed and accuracy of object detection. *arXiv preprint arXiv:2004.10934* (2020) [4](#)
4. Bolukbasi, T., Wang, J., Dekel, O., Saligrama, V.: Adaptive neural networks for efficient inference. In: *International Conference on Machine Learning*. pp. 527–536. PMLR (2017) [4](#)
5. Carion, N., Massa, F., Synnaeve, G., Usunier, N., Kirillov, A., Zagoruyko, S.: End-to-end object detection with transformers. In: *European conference on computer vision*. pp. 213–229. Springer (2020) [4](#), [6](#)
6. Caron, M., Touvron, H., Misra, I., Jégou, H., Mairal, J., Bojanowski, P., Joulin, A.: Emerging properties in self-supervised vision transformers. In: *Proceedings of the IEEE/CVF international conference on computer vision*. pp. 9650–9660 (2021) [3](#), [4](#)
7. Chen, Y., Dai, X., Liu, M., Chen, D., Yuan, L., Liu, Z.: Dynamic relu. In: *European Conference on Computer Vision*. pp. 351–367. Springer (2020) [4](#)
8. Chen, Y., Li, Y., Kong, T., Qi, L., Chu, R., Li, L., Jia, J.: Scale-aware automatic augmentation for object detection. In: *Proceedings of the IEEE/CVF conference on computer vision and pattern recognition*. pp. 9563–9572 (2021) [1](#), [2](#), [4](#), [7](#), [13](#)
9. Coello, C.A.C.: *Evolutionary algorithms for solving multi-objective problems*. Springer (2007) [2](#), [7](#)
10. Cubuk, E.D., Zoph, B., Mane, D., Vasudevan, V., Le, Q.V.: Autoaugment: Learning augmentation policies from data. *arXiv preprint arXiv:1805.09501* (2018) [4](#)
11. Cubuk, E.D., Zoph, B., Shlens, J., Le, Q.V.: Randaugment: Practical automated data augmentation with a reduced search space. In: *Proceedings of the IEEE/CVF conference on computer vision and pattern recognition workshops*. pp. 702–703 (2020) [4](#)
12. Dai, J., Qi, H., Xiong, Y., Li, Y., Zhang, G., Hu, H., Wei, Y.: Deformable convolutional networks. In: *Proceedings of the IEEE international conference on computer vision*. pp. 764–773 (2017) [4](#)

13. Dai, X., Kong, X., Guo, T.: Epnet: Learning to exit with flexible multi-branch network. In: Proceedings of the 29th ACM International Conference on Information & Knowledge Management. pp. 235–244 (2020) [4](#)
14. Dai, X., Chen, Y., Xiao, B., Chen, D., Liu, M., Yuan, L., Zhang, L.: Dynamic head: Unifying object detection heads with attentions. In: Proceedings of the IEEE/CVF conference on computer vision and pattern recognition. pp. 7373–7382 (2021) [4](#)
15. Everingham, M., Van Gool, L., Williams, C.K., Winn, J., Zisserman, A.: The pascal visual object classes (voc) challenge. *International journal of computer vision* **88**, 303–338 (2010) [3](#)
16. Gao, H., Zhu, X., Lin, S., Dai, J.: Deformable kernels: Adapting effective receptive fields for object deformation. *arXiv preprint arXiv:1910.02940* (2019) [4](#)
17. Ghiasi, G., Lin, T.Y., Le, Q.V.: Nas-fpn: Learning scalable feature pyramid architecture for object detection. In: Proceedings of the IEEE/CVF conference on computer vision and pattern recognition. pp. 7036–7045 (2019) [3](#)
18. Girshick, R.: Fast r-cnn. In: Proceedings of the IEEE international conference on computer vision. pp. 1440–1448 (2015) [4](#)
19. Han, J., Ding, J., Xue, N., Xia, G.S.: Redet: A rotation-equivariant detector for aerial object detection. In: Proceedings of the IEEE/CVF Conference on Computer Vision and Pattern Recognition. pp. 2786–2795 (2021) [10](#), [11](#)
20. Han, Y., Huang, G., Song, S., Yang, L., Wang, H., Wang, Y.: Dynamic neural networks: A survey. *IEEE Transactions on Pattern Analysis and Machine Intelligence* **44**(11), 7436–7456 (2021) [4](#)
21. Hao, Z., Liu, Y., Qin, H., Yan, J., Li, X., Hu, X.: Scale-aware face detection. In: Proceedings of the IEEE Conference on Computer Vision and Pattern Recognition. pp. 6186–6195 (2017) [2](#), [3](#), [4](#)
22. He, K., Gkioxari, G., Dollár, P., Girshick, R.: Mask r-cnn. In: Proceedings of the IEEE international conference on computer vision. pp. 2961–2969 (2017) [4](#)
23. He, K., Zhang, X., Ren, S., Sun, J.: Deep residual learning for image recognition. In: Proceedings of the IEEE conference on computer vision and pattern recognition. pp. 770–778 (2016) [3](#)
24. Hu, J., Shen, L., Sun, G.: Squeeze-and-excitation networks. In: Proceedings of the IEEE conference on computer vision and pattern recognition. pp. 7132–7141 (2018) [4](#)
25. Hua, W., Zhou, Y., De Sa, C.M., Zhang, Z., Suh, G.E.: Channel gating neural networks. *Advances in Neural Information Processing Systems* **32** (2019) [4](#)
26. Jia, D., Yuan, Y., He, H., Wu, X., Yu, H., Lin, W., Sun, L., Zhang, C., Hu, H.: Detsr with hybrid matching. In: Proceedings of the IEEE/CVF Conference on Computer Vision and Pattern Recognition. pp. 19702–19712 (2023) [3](#), [4](#)
27. Lee, H., Kim, H.E., Nam, H.: Srm: A style-based recalibration module for convolutional neural networks. In: Proceedings of the IEEE/CVF International conference on computer vision. pp. 1854–1862 (2019) [4](#)
28. Li, S., Yang, L., Huang, J., Hua, X.S., Zhang, L.: Dynamic anchor feature selection for single-shot object detection. In: Proceedings of the IEEE/CVF international conference on computer vision. pp. 6609–6618 (2019) [4](#)
29. Li, Y., Chen, Y., Wang, N., Zhang, Z.: Scale-aware trident networks for object detection. In: Proceedings of the IEEE/CVF international conference on computer vision. pp. 6054–6063 (2019) [1](#)
30. Lin, T.Y., Dollár, P., Girshick, R., He, K., Hariharan, B., Belongie, S.: Feature pyramid networks for object detection. In: Proceedings of the IEEE conference on computer vision and pattern recognition. pp. 2117–2125 (2017) [1](#), [3](#)

31. Lin, T.Y., Goyal, P., Girshick, R., He, K., Dollár, P.: Focal loss for dense object detection. In: Proceedings of the IEEE international conference on computer vision. pp. 2980–2988 (2017) [3](#), [4](#)
32. Lin, T.Y., Maire, M., Belongie, S., Hays, J., Perona, P., Ramanan, D., Dollár, P., Zitnick, C.L.: Microsoft coco: Common objects in context. In: Computer Vision–ECCV 2014: 13th European Conference, Zurich, Switzerland, September 6–12, 2014, Proceedings, Part V 13. pp. 740–755. Springer (2014) [3](#)
33. Lin, Z., Wang, Y., Zhang, J., Chu, X.: Dynamicdet: A unified dynamic architecture for object detection. In: Proceedings of the IEEE/CVF Conference on Computer Vision and Pattern Recognition. pp. 6282–6291 (2023) [4](#)
34. Liu, S., Qi, L., Qin, H., Shi, J., Jia, J.: Path aggregation network for instance segmentation. In: Proceedings of the IEEE conference on computer vision and pattern recognition. pp. 8759–8768 (2018) [1](#), [3](#)
35. Liu, W., Anguelov, D., Erhan, D., Szegedy, C., Reed, S., Fu, C.Y., Berg, A.C.: Ssd: Single shot multibox detector. In: Computer Vision–ECCV 2016: 14th European Conference, Amsterdam, The Netherlands, October 11–14, 2016, Proceedings, Part I 14. pp. 21–37. Springer (2016) [1](#), [2](#), [4](#)
36. Liu, Z., Hu, H., Lin, Y., Yao, Z., Xie, Z., Wei, Y., Ning, J., Cao, Y., Zhang, Z., Dong, L., et al.: Swin transformer v2: Scaling up capacity and resolution. In: Proceedings of the IEEE/CVF conference on computer vision and pattern recognition. pp. 12009–12019 (2022) [2](#)
37. Liu, Z., Lin, Y., Cao, Y., Hu, H., Wei, Y., Zhang, Z., Lin, S., Guo, B.: Swin transformer: Hierarchical vision transformer using shifted windows. In: Proceedings of the IEEE/CVF international conference on computer vision. pp. 10012–10022 (2021) [2](#)
38. Long, J., Shelhamer, E., Darrell, T.: Fully convolutional networks for semantic segmentation. In: Proceedings of the IEEE conference on computer vision and pattern recognition. pp. 3431–3440 (2015) [1](#)
39. Maron, O., Lozano-Pérez, T.: A framework for multiple-instance learning. Advances in neural information processing systems **10** (1997) [2](#), [7](#)
40. Micikevicius, P., Narang, S., Alben, J., Diamos, G., Elsen, E., Garcia, D., Ginsburg, B., Houston, M., Kuchaiev, O., Venkatesh, G., et al.: Mixed precision training. arXiv preprint arXiv:1710.03740 (2017) [11](#)
41. Papageorgiou, C., Poggio, T.: A trainable system for object detection. International journal of computer vision **38**, 15–33 (2000) [4](#)
42. Park, E., Kim, D., Kim, S., Kim, Y.D., Kim, G., Yoon, S., Yoo, S.: Big/little deep neural network for ultra low power inference. In: 2015 International Conference on Hardware/Software Codesign and System Synthesis (CODES+ ISSS). pp. 124–132. IEEE (2015) [4](#)
43. Redmon, J., Divvala, S., Girshick, R., Farhadi, A.: You only look once: Unified, real-time object detection. In: Proceedings of the IEEE conference on computer vision and pattern recognition. pp. 779–788 (2016) [1](#), [4](#)
44. Ren, S., He, K., Girshick, R., Sun, J.: Faster r-cnn: Towards real-time object detection with region proposal networks. Advances in neural information processing systems **28** (2015) [3](#), [4](#)
45. Ren, T., Liu, S., Li, F., Zhang, H., Zeng, A., Yang, J., Liao, X., Jia, D., Li, H., Cao, H., Wang, J., Zeng, Z., Qi, X., Yuan, Y., Yang, J., Zhang, L.: detrex: Benchmarking detection transformers (2023) [11](#)
46. Singh, B., Davis, L.S.: An analysis of scale invariance in object detection snip. In: Proceedings of the IEEE conference on computer vision and pattern recognition. pp. 3578–3587 (2018) [1](#), [2](#), [4](#)

47. Singh, B., Najibi, M., Davis, L.S.: Sniper: Efficient multi-scale training. *Advances in neural information processing systems* **31** (2018) 1, 4
48. Tan, M., Le, Q.: Efficientnet: Rethinking model scaling for convolutional neural networks. In: *International conference on machine learning*. pp. 6105–6114. PMLR (2019) 2, 3
49. Tan, M., Pang, R., Le, Q.V.: Efficientdet: Scalable and efficient object detection. In: *Proceedings of the IEEE/CVF conference on computer vision and pattern recognition*. pp. 10781–10790 (2020) 2
50. Tian, R., Wu, Z., Dai, Q., Hu, H., Qiao, Y., Jiang, Y.G.: Resformer: Scaling vits with multi-resolution training. In: *Proceedings of the IEEE/CVF Conference on Computer Vision and Pattern Recognition*. pp. 22721–22731 (2023) 2
51. Tian, Z., Chen, H., Wang, X., Liu, Y., Shen, C.: AdelaiDet: A toolbox for instance-level recognition tasks. <https://git.io/adelaidet> (2019) 11
52. Tian, Z., Shen, C., Chen, H., He, T.: Fcos: Fully convolutional one-stage object detection. In: *Proceedings of the IEEE/CVF international conference on computer vision*. pp. 9627–9636 (2019) 3, 4, 6
53. Vaswani, A., Shazeer, N., Parmar, N., Uszkoreit, J., Jones, L., Gomez, A.N., Kaiser, Ł., Polosukhin, I.: Attention is all you need. *Advances in neural information processing systems* **30** (2017) 4
54. Wang, C.Y., Bochkovskiy, A., Liao, H.Y.M.: Scaled-yolov4: Scaling cross stage partial network. In: *Proceedings of the IEEE/cvf conference on computer vision and pattern recognition*. pp. 13029–13038 (2021) 11
55. Wang, C.Y., Bochkovskiy, A., Liao, H.Y.M.: Yolov7: Trainable bag-of-freebies sets new state-of-the-art for real-time object detectors. In: *Proceedings of the IEEE/CVF Conference on Computer Vision and Pattern Recognition*. pp. 7464–7475 (2023) 4
56. Wang, H., Kembhavi, A., Farhadi, A., Yuille, A.L., Rastegari, M.: Elastic: Improving cnns with dynamic scaling policies. In: *Proceedings of the IEEE/CVF Conference on Computer Vision and Pattern Recognition*. pp. 2258–2267 (2019) 1, 4
57. Wang, J., Chen, K., Yang, S., Loy, C.C., Lin, D.: Region proposal by guided anchoring. In: *Proceedings of the IEEE/CVF conference on computer vision and pattern recognition*. pp. 2965–2974 (2019) 1, 4
58. Wang, X., Luo, Y., Crankshaw, D., Tumanov, A., Yu, F., Gonzalez, J.E.: Idk cascades: Fast deep learning by learning not to overthink. *arXiv preprint arXiv:1706.00885* (2017) 4
59. Wu, Y., Kirillov, A., Massa, F., Lo, W.Y., Girshick, R.: Detectron2. <https://github.com/facebookresearch/detectron2> (2019) 11
60. Xia, G.S., Bai, X., Ding, J., Zhu, Z., Belongie, S., Luo, J., Datcu, M., Pelillo, M., Zhang, L.: Dota: A large-scale dataset for object detection in aerial images. In: *Proceedings of the IEEE conference on computer vision and pattern recognition*. pp. 3974–3983 (2018) 3
61. Xie, S., Girshick, R., Dollár, P., Tu, Z., He, K.: Aggregated residual transformations for deep neural networks. In: *Proceedings of the IEEE conference on computer vision and pattern recognition*. pp. 1492–1500 (2017) 3
62. Yang, Z., Liu, S., Hu, H., Wang, L., Lin, S.: Reppoints: Point set representation for object detection. In: *Proceedings of the IEEE/CVF international conference on computer vision*. pp. 9657–9666 (2019) 4
63. Zhang, H., Zhang, P., Hu, X., Chen, Y.C., Li, L., Dai, X., Wang, L., Yuan, L., Hwang, J.N., Gao, J.: Glipv2: Unifying localization and vision-language under-

- standing. *Advances in Neural Information Processing Systems* **35**, 36067–36080 (2022) [2](#)
64. Zhang, S., Chi, C., Yao, Y., Lei, Z., Li, S.Z.: Bridging the gap between anchor-based and anchor-free detection via adaptive training sample selection. In: *Proceedings of the IEEE/CVF conference on computer vision and pattern recognition*. pp. 9759–9768 (2020) [4](#)
65. Zhang, X., Wan, F., Liu, C., Ji, R., Ye, Q.: Freeanchor: Learning to match anchors for visual object detection. *Advances in neural information processing systems* **32** (2019) [7](#), [8](#)
66. Zhou, H.Y., Gao, B.B., Wu, J.: Adaptive feeding: Achieving fast and accurate detections by adaptively combining object detectors. In: *Proceedings of the IEEE International Conference on Computer Vision*. pp. 3505–3513 (2017) [4](#)
67. Zhu, L., Deng, Z., Hu, X., Fu, C.W., Xu, X., Qin, J., Heng, P.A.: Bidirectional feature pyramid network with recurrent attention residual modules for shadow detection. In: *Proceedings of the European Conference on Computer Vision (ECCV)*. pp. 121–136 (2018) [3](#)
68. Zhu, M., Han, K., Wu, E., Zhang, Q., Nie, Y., Lan, Z., Wang, Y.: Dynamic resolution network. *Advances in Neural Information Processing Systems* **34**, 27319–27330 (2021) [2](#), [4](#)
69. Zhu, X., Hu, H., Lin, S., Dai, J.: Deformable convnets v2: More deformable, better results. In: *Proceedings of the IEEE/CVF conference on computer vision and pattern recognition*. pp. 9308–9316 (2019) [4](#)
70. Zhu, X., Su, W., Lu, L., Li, B., Wang, X., Dai, J.: Deformable detr: Deformable transformers for end-to-end object detection. *arXiv preprint arXiv:2010.04159* (2020) [4](#)